Improving the Stable Surface Layer in the NCEP Global Forecast System

WEIZHONG ZHENG

NOAA/NCEP/Environmental Modeling Center, and I.M. Systems Group, Inc., NOAA/NCEP/Environmental Modeling Center, College Park, Maryland

MICHAEL EK

NOAA/NCEP/Environmental Modeling Center, College Park, Maryland

KENNETH MITCHELL

Prescient Weather Ltd., State College, Pennsylvania

HELIN WEI AND JESSE MENG

NOAA/NCEP/Environmental Modeling Center, and I.M. Systems Group, Inc., NOAA/NCEP/Environmental Modeling Center, College Park, Maryland

(Manuscript received 21 November 2016, in final form 26 June 2017)

ABSTRACT

This study examines the performance of the NCEP Global Forecast System (GFS) surface layer parameterization scheme for strongly stable conditions over land in which turbulence is weak or even disappears because of high near-surface atmospheric stability. Cases of both deep snowpack and snow-free conditions are investigated. The results show that decoupling and excessive near-surface cooling may appear in the late afternoon and nighttime, manifesting as a severe cold bias of the 2-m surface air temperature that persists for several hours or more. Concurrently, because of negligible downward heat transport from the atmosphere to the land, a warm temperature bias develops at the first model level. The authors test changes to the stable surface layer scheme that include introduction of a stability parameter constraint that prevents the land–atmosphere system from fully decoupling and modification to the roughness-length formulation. GFS sensitivity runs with these two changes demonstrate the ability of the proposed surface layer changes to reduce the excessive near-surface cooling in forecasts of 2-m surface air temperature. The proposed changes prevent both the collapse of turbulence in the stable surface layer over land and the possibility of numerical instability resulting from thermal decoupling between the atmosphere and the surface. The authors also execute and evaluate daily GFS 7-day test forecasts with the proposed changes spanning a one-month period in winter. The assessment reveals that the systematic deficiencies and substantial errors in GFS near-surface 2-m air temperature forecasts are considerably reduced, along with a notable reduction of temperature errors throughout the lower atmosphere and improvement of forecast skill scores for light and medium precipitation amounts.

1. Introduction

In numerical weather and climate models, the lowest model layer is usually considered to be the surface layer, through which atmospheric forcing from the parent atmospheric model drives a land surface model, while the land surface model in turn provides the lower boundary conditions to the atmospheric model. Also, in the data assimilation systems that provide initial conditions for atmospheric forecast models, the land surface skin temperature is a critical surface field for the assimilation of satellite radiance observations, especially observations in so-called window channels that are sensitive to the state of the earth surface (Zheng et al. 2012).

Thus, the surface layer parameterization strongly influences both 1) the land–atmospheric coupling "strength" and 2) the surface heat and momentum fluxes, land surface skin temperature, and the near-surface air temperature, hence the parameterization serves a critical role in numerical weather and climate prediction (Santanello et al. 2009; van den Hurk et al. 2011; Dirmeyer et al. 2012).

Corresponding author: Weizhong Zheng, weizhong.zheng@noaa.gov

DOI: 10.1175/MWR-D-16-0438.1

Despite several decades of research into surface layer treatments in numerical models, ongoing challenges remain in parameterizing the very stable surface layer, owing to a high sensitivity arising from the small magnitudes of the vertical heat fluxes composing the heat budget of the very stable surface layer (Fernando and Weil 2010; Holtslag et al. 2013; Mahrt 2014; Medeiros and Fitzjarrald 2014; Steeneveld 2014).

A problem common to surface layer parameterization is related to the Monin–Obukhov (MO) similarity hypothesis, which describes (as presented in the appendix) the vertical behavior of nondimensionalized mean flow and turbulence properties within the surface layer (Monin and Obukhov 1954). In spite of its widespread use, MO similarity theory has limitations, such as its difficulty in properly reproducing turbulent fluxes in the very stable regime, or even the intermediate stable regime (Zilitinkevich and Calanca 2000;Holtslag et al. 2007; Fernando and Weil 2010; Van de Wiel et al. 2012a,b; Vihma et al. 2014; Mahrt 2014, Grachev et al. 2013, 2015). Consequently, the stable boundary layer overall remains inadequately represented in weather and climate models (Sandu et al. 2013; Steeneveld 2014).

The deficiencies in parameterizations of the very stable boundary layer in weather and climate models may result in excessive cold bias and even collapse of turbulence with unrealistic decoupling of the atmosphere from the surface (e.g., Derbyshire 1999; Mahrt et al. 1998; Van de Wiel et al. 2012a,b; Mahrt 2014; Couvreux et al. 2016). Some other models show a possible warm bias of surface temperature during calm nights (Atlaskin and Vihma 2012). In addition to the condition of weak turbulence, decoupling largely depends on land surface parameters like surface roughness and soil thermal diffusivity (Derbyshire 1999). Using a simple bulk-model analog to the stably stratified case, Van de Wiel et al. (2007, 2012a,b) studied the mechanism behind the collapse of turbulence in the nocturnal boundary layer. Their analytical theory derives a critical value associated with the surface roughness length for momentum and shows that a collapse of turbulence can occur when a certain critical value of the MO stability parameter is exceeded.

Users of the NCEP Global Forecast System (GFS), as well as verification of GFS forecasts performed in the Environmental Modeling Center (EMC) of NCEP, have long reported large errors in GFS forecasts of near-surface air temperature in some regions and seasons (e.g., Freedman and Ek 2004; Atlaskin and Vihma 2012; Bosveld et al. 2014). In particular, severe cold biases of 2-m air temperature typically occur in the late afternoon and nighttime, especially during spring, autumn, and winter, which suggests the biases are related to the transitional period from daytime unstable boundary layer conditions to nocturnal stable conditions.

There are many factors that may contribute to such cold biases in model forecasts of near-surface air temperature in stable boundary layers, such as horizontal advection, representation of clouds in the boundary layer (Sandu et al. 2013), and, especially, vertical turbulent mixing. The vertical turbulent mixing associated with subgrid-scale land surface heterogeneity, gravity waves, and subgrid-scale motions such as cold air drainage is usually omitted in numerical models (Mahrt 2008; Stoll and Porté-Agel 2009; Steeneveld et al. 2010; Steeneveld 2011). However, in the real world, such sources of vertical mixing sometimes represent the dominant source of generating turbulence in very stable boundary layers, which arise from strong net radiative cooling of the surface or by the flow of warm low-level air over much cooler surfaces, such as snow-covered surfaces. In such very stable boundary layers, the weak and typically intermittent turbulence generally fails to achieve equilibrium with the constantly changing submesoscale motions (Mahrt 2014). To compensate for errors caused by the poor or omitted representation of these processes in numerical models, several approaches have been applied to reduce the cold near-surface temperature bias over land (Sandu et al. 2013; Holtslag et al. 2013; Steeneveld 2014). For example, at the European Centre for Medium-Range Weather Forecasts (ECMWF), the turbulent diffusion in stable conditions was artificially enhanced to eliminate to a large extent the systematic 2-m air temperature biases in winter seasons (Viterbo et al. 1999).

This paper examines the behavior of the GFS parameterization scheme for the stable surface layer over land, especially for the very stable condition, to investigate the severe cold biases of the GFS 2-m air temperature forecasts. Moreover, daily GFS 7-day test forecasts spanning a 1-month period are executed to determine if the proposed approaches improve GFS 2-m air temperature forecasts consistently throughout a full month of daily forecasts.

The paper is organized as follows: in section 2 the NCEP GFS model and Noah land surface model are briefly described. The parameterization of and our proposed changes to the GFS stable surface layer are presented in section 3. Section 4 presents results from GFS simulations in two forecast cases applying our proposed approaches in the surface layer scheme. The results for one month of daily winter forecasts using the proposed approaches are given in section 5. Finally, the conclusions from this study are presented in section 6.

2. NCEP GFS model and Noah land surface model

The NCEP GFS is the operational NCEP global spectral numerical forecast model [and its associated ensemble Kalman filter (EnKF) hybrid data assimilation system providing the initial states] based on the primitive dynamical equations for the fluid dynamics and a suite of parameterizations for atmospheric physics. There have been substantial recent updates of the operational GFS, such as adoption of semi-Lagrangian dynamics and higher horizontal resolution (T1534). The Noah land surface model is coupled to the GFS and, along with the GFS surface layer scheme, determines the heat, moisture, and momentum exchanges between the land surface and the atmosphere. The Noah land surface model has four soil layers, a linearized surface energy budget formulation that can be explicitly solved for the land surface skin temperature (Ek 2004) and applies several input land datasets such as soil and vegetation type, a seasonally varying green vegetation fraction, snow-free albedo, and maximum snow albedo (Ek et al. 2003).

In parameterizing the planetary boundary layer, the currently operational GFS applies the hybrid eddy-diffusivity mass-flux (EDMF) planetary boundary layer scheme that includes dissipative heating and modified stable boundary layer mixing (Han et al. 2016). This EDMF scheme replaces the former GFS nonlocal first-order mixing scheme, which included stratocumulus-top-driven turbulence mixing (Troen and Mahrt 1986; Hong and Pan 1996; Han and Pan 2011). In the surface layer, the GFS applies the MO similarity profile scheme with modified stability functions (Miyakoda and Sirutis 1986; Long 1984, 1986). Momentum and thermal roughness lengths are necessary to estimate the surface fluxes from the atmospheric surface layer similarity theory. In the current operational GFS, the momentum roughness length z_{0M} is specified according to the fixed vegetation types but has no seasonal variation. The thermal roughness length z_{0H} is derived by a seasonally varying formulation dependent on the seasonal cycle of green vegetation fraction (Zheng et al. 2012). In this z_{0H} formulation, a key parameter known as C_{zil} is specified according to a dependence on canopy height, as described in section 3b.

3. Surface layer stable condition

In the GFS model, the parameterization of turbulent fluxes for momentum, heat, and moisture within the stable surface layer was developed by Long (1986), based on the surface layer scheme in the Geophysical Fluid Dynamics Laboratory's "E2" physics package (Miyakoda and Sirutis 1986). Unlike many other schemes that impose an upper bound on the permitted magnitude of the stable bulk Richardson number, this parameterization scheme uses an alternative flux-profile formulation that imposes no critical bulk Richardson number, that is, it has no limitation of a finite critical bulk Richardson number throughout a continuous range of the stable regime. The appendix briefly presents the features of this scheme.

a. Introduction of a stability parameter constraint

During nighttime, there is no shortwave radiation and almost no surface latent heat flux (evaporation), so the nighttime surface energy balance is typically reduced to the net longwave radiation at the surface (difference of downward and outgoing longwave radiation at the surface) being balanced by the sum of ground heat flux and sensible heat flux. Other subgrid-scale nonturbulent motions (such as cold-air drainage) can affect the actual surface energy budget, but such nonturbulent motions are usually small and typically omitted in numerical models (Mahrt 2014). However, for the very stable regime, the surface sensible heat flux can also be very small. Therefore, the surface energy balance in very stable conditions can exhibit a distinctly different behavior and sensitivity owing to the turbulence being very weak or virtually nonexistent. Under such very stable conditions, the surface energy budget in models has a high likelihood of reducing to the net longwave radiation at the surface being balanced merely by the ground heat flux. Hence, the subgrid-scale nonturbulent motions may no longer be negligible in the surface energy budget (e.g., over deep snowpack where the ground heat flux can also be very small). The solution of surface skin temperature from the surface energy balance may be a very different equilibrium state from the one of nonnegligible turbulence (Derbyshire 1999; Van de Wiel et al. 2002a, b). We explore this possibility further below.

Derbyshire (1999) considered a very stable case under a clear night and illustrated that two different stable boundary responses were possible because of the strong surface radiative cooling. One response is a negative feedback whereby the surface cooling decreases the surface temperature that, in turn, increases the vertical temperature gradient and generates more downward sensible heat flux, which augments the ground heat flux to balance the next longwave radiative cooling, so the drop in surface skin surface substantially moderates. This type of boundary layer response stabilizes the coupled land–atmosphere system and has one quasi–steady state. The second response is a positive feedback whereby the increase of the vertical temperature gradient resulting from the surface cooling increases the atmospheric stability and suppresses the

turbulent sensible heat flux, even ultimately to zero, so that there is very weak or no downward sensible heat flux to compensate for the radiative surface cooling. So ultimately, the land surface temperature drops much further until the increase in the ground heat flux from the increased soil temperature gradient is sufficient to balance the net surface longwave radiation. If substantial snowpack is present, the land surface temperature drop is even more extreme because the insulating effect of the snowpack suppresses the ground/subsurface heat flux. This second type of very stable boundary layer response leads the coupled land–atmosphere system to a dramatically different regime that results in very excessive cooling of the land surface, and hence results in excessive cooling of the 2-m air temperature, which is diagnosed from the land surface temperature and the lowest model level atmospheric temperature.

Therefore, it is clear that in order to derive a suitable equilibrium solution for the very stable surface layer, the surface energy balance needs to include other independent forcings, even if indirectly. One such alternative approach is to prevent the collapse of turbulence and avoid a positive feedback in the boundary layer. Van de Wiel et al. (2007) used a simple flow analogy of stably stratified atmospheric flow to study the collapse of turbulence and indicated that the system has a marginal state or a ''turning'' point expressed by a critical value of the MO stability parameter $(z/L)_{\rm lim}$, according to a linear analytical theory. This turning point separates numerically unstable from numerically stable solutions, and beyond it no equilibrium solution exists. Therefore, this turning point predicts a collapse of turbulence when a certain value of the MO stability parameter z/L is exceeded.

For real and complicated atmospheric stratified flows in numerical models such as the GFS, it is difficult to analytically derive such a turning point value of $(z/L)_{\rm lim}$. Thus, the simple approach in this study is to employ the linear theory expression of Van de Wiel et al. (2007) in Eq. (A13) as follows:

$$(z/L)_{\rm lim} = \frac{\ln\left(\frac{z}{z_{0M}}\right)}{2\alpha\left(1-\frac{z_{0M}}{z}\right)}. \qquad (1)$$

Use of the above limitation of the MO stability parameter in the surface layer stable conditions basically implies only considering cases in which sensible heat flux is proportional to the temperature difference (Basu et al. 2008; Gibbs et al. 2015). Following Basu's method (Basu et al. 2008), Fig. 1 provides examples of the iterative solutions for the friction velocity u_* versus the negative sensible heat flux $-\langle w\theta\rangle$ by using the Dyer (1974) form of φ and the form of φ in the GFS [Eq. (A12)], respectively. Compared to the Dyer form, the GFS form exhibits lower z/L and higher u_* as $-\langle w\theta\rangle$ increases. The GFS control run leads to the numerically unstable iterative solutions of u_* if $-\langle w\theta\rangle$ is larger than the maximum achievable sensible heat flux $-\langle w\theta\rangle_M$. With the stability parameter constraint in Eq. (1), the GFS experimental runs show the numerically stable iterative solutions for u_* under large negative sensible heat flux conditions with the minimum friction velocity sustained near or above $-\langle w\theta\rangle_M$.

The iterative solution for u_* is sensitive to the height z (i.e., the height of the first model level). As illustrated in Fig. 1, reduction of this height from 20 to 10 m increases the maximum achievable sensible heat flux $-\langle w\theta\rangle_M$, implying that a finer vertical model grid can reduce the chances of a nonexistent real solution for u_*. However, the numerically unstable iterative solutions of u_* still remain when the negative sensible heat flux is larger than $-\langle w\theta\rangle_M$ and thus the constraint on the MO stability parameter in Eq. (1) is still necessary to avoid the numerically unstable solutions.

In the modified GFS surface layer parameterization scheme tested here, the MO stability parameter z/L is limited by the value $(z/L)_{\rm lim}$ in Eq. (1) under stable conditions, so the collapse of turbulence is prevented for the very stable case, as shown by experiments in the next section. It should be noted that use of this limitation implies that the model is only able to capture the near-neutral to weakly stable regime.

b. *Introduction of seasonality to the roughness length and revised parameter $C_{\rm zil}$*

As mentioned in the introduction, the surface roughness length for momentum is an important parameter affecting the land–atmosphere interaction and turbulence behavior. In the current GFS model, z_{0M} is fixed in time and its value is assigned for each vegetation class, as shown in Table 1. However, many estimates of surface roughness length for momentum reveal a large temporal variability, most apparently in arid and semiarid regions over the globe (e.g., Hagemann 2002; Prigent et al. 2005). Thus, seasonal variations of surface roughness length for momentum are expected especially over the western continental United States (CONUS), which is primarily covered by grassland, broadleaf shrubs, or cultivated areas, as well as over the cultivated portions of the eastern CONUS.

Furthermore, the treatment of thermal roughness length z_{0H} has been demonstrated to significantly affect estimates of the surface exchange coefficient for heat and the forecast of the land surface skin temperature,

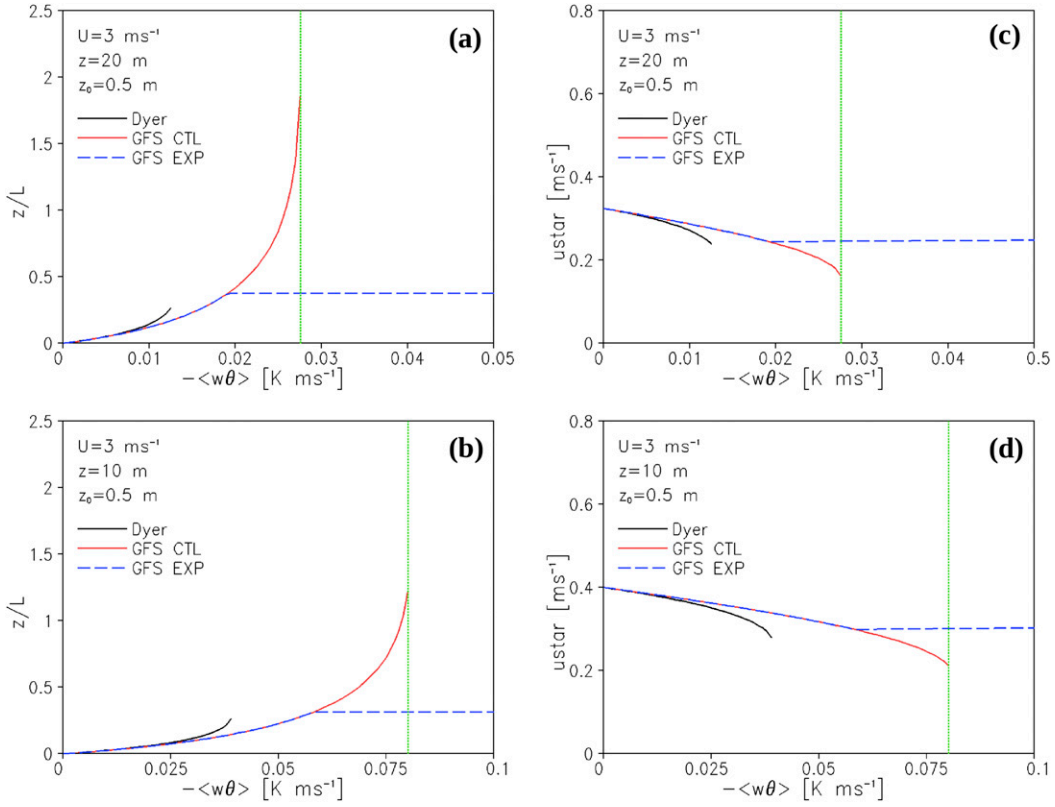

FIG. 1. (right) Iterative solutions for friction velocity u_* (m s^{-1}) as a function of negative sensible heat flux $-\langle w\theta\rangle$ (K m s^{-1}) by using the Dyer (1974) form of φ (black) and the form of φ in the GFS. (left) The MO stability parameter z/L as a function of negative sensible heat flux. GFS EXP (blue) and GFS CTL (red) denote iterative solutions with and without the stability parameter constraint, respectively. The dashed vertical lines (green) indicate the maximum achievable sensible heat flux $-\langle w\theta\rangle_M$ for GFS CTL. The reference potential temperature is assumed 270 K in all these tests.

especially over the arid and semiarid regions in the warm season (Zheng et al. 2012). For the vegetation-dependent formulation of thermal roughness length in the current GFS model, a critical parameter known as C_{zil} (Brutsaert 1975; Zilitinkevich 1995) used in the determination of the ratio of momentum roughness length to *thermal* roughness length is an empirical coefficient and assigned different values as a function of canopy height h (Chen and Zhang 2009), where h is taken as $z_{0M}/0.07$. As seen in Table 1, C_{zil} values for most

TABLE 1. Summary of values of surface roughness length for momentum z_{0M} (m) and the C_{zil} parameter as function of vegetation class for the control run and the experiments.

Vegetation class	CTL: z_{0M}	EXP: z_{0M_max}	EXP: z_{0M_min}	CTL: C_{zil}	EXP: C_{zil}
Broadleaf evergreen trees	2.653	0.500	0.500	0.000	0.8
Broad deciduous trees	0.826	0.500	0.500	0.000	0.8
Broadleaf and needleleaf trees	0.563	0.500	0.500	0.001	0.8
Needleleaf evergreen trees	1.089	0.500	0.500	0.000	0.8
Needleleaf deciduous trees	0.854	0.500	0.500	0.000	0.8
Broadleaf trees with ground cover	0.856	0.150	0.150	0.000	0.8
Groundcover only	0.035	0.120	0.100	0.631	0.8
Broadleaf shrubs with groundcover	0.238	0.050	0.010	0.044	0.8
Broadleaf shrubs with bare soil	0.065	0.060	0.010	0.425	0.8
Dwarf trees and shrubs with groundcover	0.076	0.150	0.150	0.368	0.8
Bare soil	0.011	0.010	0.010	0.865	0.8
Cultivations	0.035	0.150	0.050	0.631	0.8
Glacial	0.011	0.001	0.001	0.865	0.8

vegetation categories are much smaller than the 0.8 value used in Zheng et al. (2012). The C_{zil} values for grassland (class 7), broadleaf shrubs (class 8), and cultivations (class 12) are 0.631, 0.044, and 0.631, respectively. These three vegetation categories with small green vegetation fraction dominate the western CONUS. According to the MO similarity theory, z_{0H} is considered as the roughness height at which the logarithmic profile of potential temperature within the surface layer reaches the surface value of the potential temperature. Small C_{zil} leads to high thermal roughness length z_{0H}, thus increases the surface exchange coefficient C_H, and consequently results in large surface heat flux (Long 1984, 1986). For example, the higher z_{0H} over the arid western CONUS results in more surface heat flux during daytime and a cold bias of daytime land surface skin temperature (Zheng et al. 2012).

In this study, in addition to the new stable-case constraint of $(z/L)_{lim}$ in Eq. (1), the time-invariant value of z_{0M} for each vegetation class employed in the current GFS is replaced with a seasonally varying z_{0M} value that is obtained by temporal interpolation between a summer and winter value for each vegetation class (as shown in Table 1). Moreover, in our GFS tests here, the C_{zil} parameter is simply taken as the constant 0.8 (Zheng et al. 2012), replacing the dependence of the C_{zil} parameter on vegetation canopy height in the current operational GFS to reduce a cold bias of daytime land surface skin temperature.

4. Two forecast test cases

A series of five GFS experiments (EXP) are performed to examine the impacts of the changes described in sections 3a and 3b. The control run (CTL) uses the current GFS operational version. EXP1 tests the impact of using both the updated z_{0M} and constant $C_{zil} = 0.8$ treatments. EXP2 applies only the updated z_{0M} treatment (leaving the treatment of the parameter C_{zil} unchanged), EXP3 applies only the change to a constant $C_{zil} = 0.8$, and EXP4 applies only the MO stability parameter constraint $(z/L)_{lim}$ according to Eq. (1). Finally, EXP5 is performed with all three changes, namely, the two changes of EXP1 plus the MO stability constraint of EXP4. Two GFS forecast cases are selected to demonstrate the impact of these modifications. One is over snowpack during Northern Hemisphere winter and one is a snow-free case in Northern Hemisphere autumn.

a. Winter case over snowpack

In an analysis from NCEP's Weather Prediction Center (WPC), a low pressure system moved from central Canada to the lower Great Lakes from 13 to 15 February 2015, and then reorganized into a coastal low off the northern mid-Atlantic coastline. A very cold Arctic air mass spread into the eastern United States behind the deepening coastal low, which continued to intensify as it moved northeastward along the coastline. The winter snowstorm associated with this low pressure system brought strong winds and heavy snow across much of the mid-Atlantic and northeastern United States. As the low pressure system moved farther northeastward away from New England, a high pressure system moved over the northeastern United States, and winds became quite weak in that region, especially near and following sundown.

From the initial conditions of 0000 UTC 16 February 2015, the GFS was executed for a 7-day forecast for the control run and the five experiments (EXP1, EXP2, EXP3, EXP4, and EXP5). The CTL exhibits unreasonably rapid cooling in some regions of the northeast United States in the late afternoon on 17 and 18 February, as evident in Figs. 2a and 2b, which show the 3-h change in the GFS predicted 2-m air temperature over the northeast United States from 2100 to 0000 UTC for these two days. Some areas show more than a 15°C drop during the 3 h before sunset. Figures 2c and 2d show the difference of 2-m temperature between the EXP5 and CTL runs, indicating that the large drop of 2-m temperature occurring over New York State and other regions in the northeastern United States is reduced by about half in EXP5. This improvement is further illustrated in Fig. 3, which provides a comparison of the 72-h hourly time series for all six runs and the verifying station observations of 2-m temperature for Utica, New York (43.074°N, 75.275°W), from 0000 UTC 16 February to 0000 UTC 19 February 2015. This site is covered by deciduous broadleaf forecast, and the z_{0M} is 0.826 m in CTL, EXP3, and EXP4, and 0.5 m in EXP1, EXP2, and EXP5. The 2-m temperature in CTL drops very fast from 2100 UTC 16 February until 0000 UTC 17 February 2015. The rapid cooling is up to 15°C during these 3 h, indicating a severe cold bias compared to the observations. It takes about 9 h to recover during the early evening. This kind of phenomenon of excessive cooling happens again on the following day (i.e., before 0000 UTC 18 February), and persists even longer (until 0900 UTC 18 February) before recovery. The sensitivity tests of EXP1, EXP2, and EXP3 show a 1–2 K reduction of cooling in the late afternoon and nighttime but still show dramatically poor behavior similar to the CTL run and very little improvement. The EXP4 and EXP5 runs are quite similar and substantially avoid the rapid temperature drop in the late afternoon and agree much more closely with the observations (although they get a little too warm in the late evening of either 17 or 18 February),

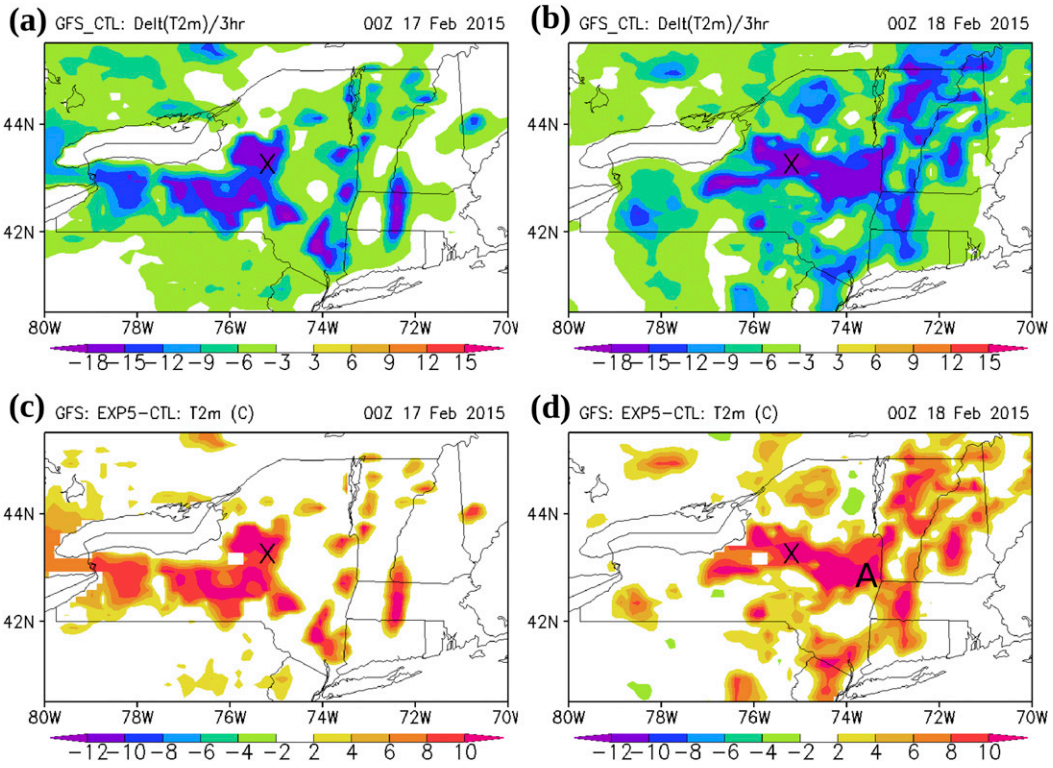

FIG. 2. The 3-h change in GFS forecasts of T_{2m} (°C) in CTL (a) from 2100 UTC 16 Feb to 0000 UTC 17 Feb 2015 and (b) from 2100 UTC 17 Feb to 0000 UTC 18 Feb 2015. Difference in T_{2m} between EXP5 and CTL at (c) 0000 UTC 17 Feb 2015, and (d) at 0000 UTC 18 Feb 2015. GFS initial conditions valid at 0000 UTC 16 Feb 2015. The "X" and "A" denote locations of Utica and Albany, NY, respectively.

indicating the MO stability parameter constraint is the most effective modification to reduce the excessive cold bias of 2-m temperature. The updated z_{0M} and constant $C_{zil} = 0.8$ treatments exhibit notable impacts on the surface skin temperature (not shown), and its verification is given later in the snow-free case in section 4b.

Figures 4a and 4b present a corresponding 72-h hourly time series of the GFS surface skin temperature T_{skin}, 2-m air temperature T_{2m}, and first model level air temperature T_{1lev} at the Utica station, for the CTL and EXP5 runs, respectively. The temperature T_{2m} is diagnosed in the GFS at 2-m height using the integrated dimensionless equation in Eq. (A8) and assuming that u_* and θ_* are constant with height. Similarly, one can derive the 10-m surface wind speed U_{10m} and 2-m specific humidity q_{2m} from the vertical profile stability functions, respectively.

For the first 24 h from 2100 UTC 16 February to 2100 UTC 17 February, these three temperatures are very close and exhibit little difference, indicating a well-mixed surface layer due to significant wind speed (see Fig. 5 below) and strong coupling between the land and the atmosphere. However, starting at 2100 UTC 17 February, when the near-surface wind is now weak as sunset approaches and solar radiation rapidly decreases then drops to zero, the land surface radiatively cools and T_{skin} rapidly drops about 17 K, while T_{1lev} does not decrease much. The difference between T_{skin} and T_{1lev} at

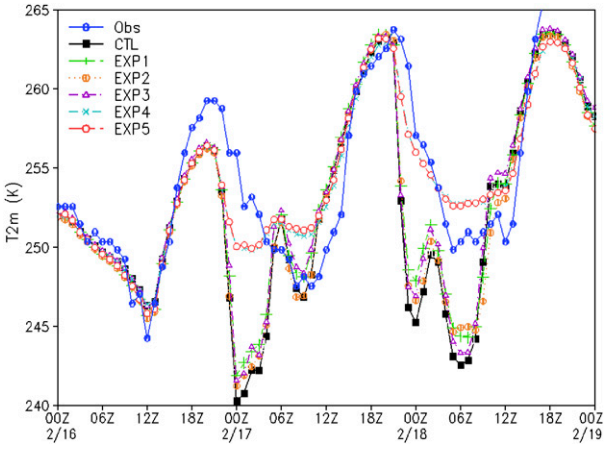

FIG. 3. Hourly time series of 2-m air temperature (K) at Utica, NY (at location of X in Fig. 2) for observations (blue), CTL (black), EXP1 (green), EXP2 (orange), EXP3 (purple), EXP4 (light blue), and EXP5 (red) during the 72-h period from 0000 UTC 16 Feb to 0000 UTC 19 Feb 2015.

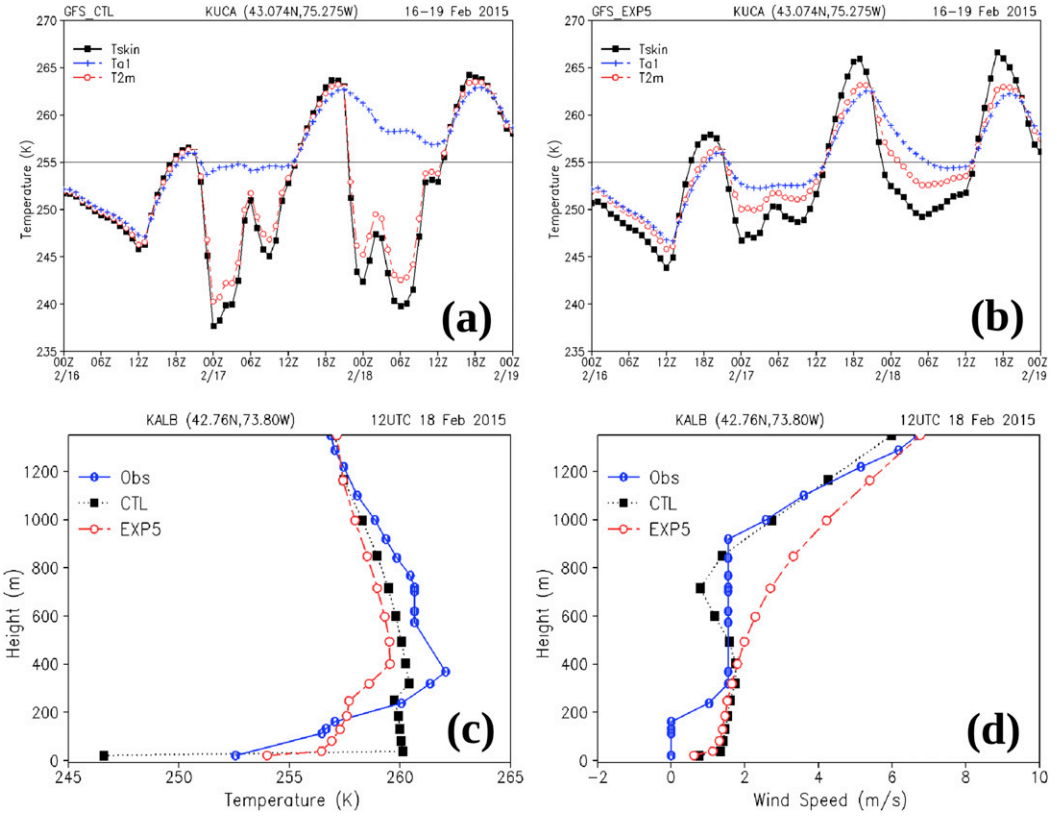

FIG. 4. Hourly time series of T_{1lev} (blue; K), T_{skin} (black; K), and T_{2m} (red; K) at Utica, NY, for (a) CTL and (b) EXP5, during the 72-h period in Fig. 3. The atmospheric (c) temperature and (d) wind speed profiles for CTL (black) and EXP5 (red) against the sounding observations (blue) at Albany, NY (at location of A in Fig. 2), at 1200 UTC 18 Feb 2015.

the first model level (21 m above the surface at this station) reaches about 16 K.

The above results indicate a decoupling in the model concurrent with a cessation of turbulent transport in the surface layer, as shown in Figs. 5a–c. Because of weak wind, a large stable vertical temperature gradient, and clear sky yielding less downward longwave flux on the surface, turbulence is weak and the friction velocity or aerodynamic conductance for momentum or heat is very small, even zero, during the period from the late afternoon of 16 February to the early evening of 17 February. Similar decoupling and unrealistic cooling appears again the next day before sunset at 0000 UTC 18 February, and the large difference between T_{skin} (or T_{2m}) and T_{1lev} is again apparent. The excessive cooling and decoupling result in a large cold bias of the surface temperatures. At the same time, owing to little downward heat transport from the atmosphere to the land, the conditions may produce a warm temperature at the first model level and at layers of the lower troposphere. Given that there is no sounding data at Utica, we utilize station data at Albany, New York (42.758°N, 73.803°W), to compare the temperature and wind profiles against the sounding observations taken at this station. A similar decoupling occurred at Albany from the late afternoon (before 0000 UTC 18 February, as shown in Fig. 2) to early morning (1200 UTC) on 18 February. Figure 4c presents a comparison of temperature profiles at 1200 UTC 18 February. The CTL run exhibits a large temperature difference near the surface, where the surface air temperature T_{2m} (246.6 K) is much lower than observed (252.6 K), while the temperatures at the lowest model level and three model levels above (below 200-m height) are several degrees higher than observed. The small downward heat transport from the atmosphere to the land during the nighttime decoupling period results in accumulation of excess heat and as a result, the warm bias exists at or above the first model level.

The EXP5 test run in Fig. 4b produces a reasonable diurnal cycle of T_{2m} (as shown in Fig. 3). Before sunset, either at 0000 UTC 17 February or at 0000 UTC 18 February, T_{skin} does not show a rapid drop and T_{1lev} decreases gradually, plus their difference is just a few degrees, indicating that the excessive cooling and decoupling between the surface and the atmosphere does

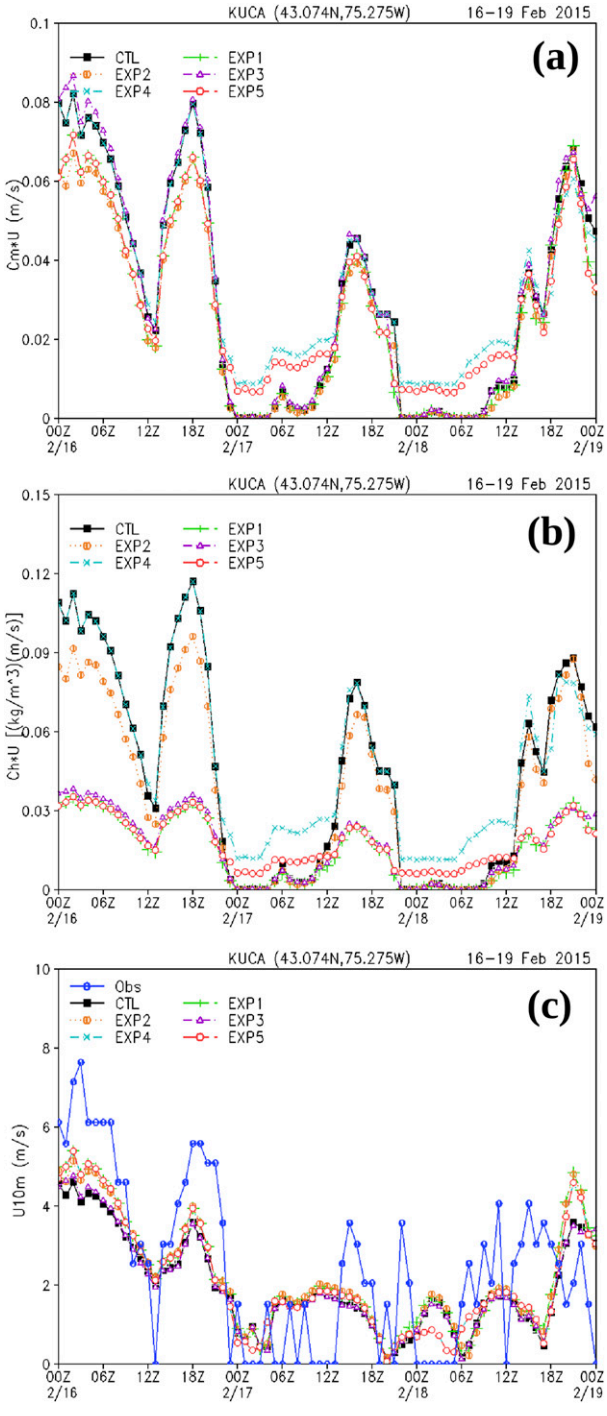

FIG. 5. Hourly time series at Utica, NY, for (a) surface aerodynamic conductance for momentum ($m\,s^{-1}$) and (b) heat ($kg\,m^{-3}\,m\,s^{-1}$), and (c) wind speed at 10 m ($m\,s^{-1}$) for observations (blue), CTL (black), EXP1 (green), EXP2 (orange), EXP3 (purple), EXP4 (light blue), and EXP5 (red) during the 72-h period in Fig. 3.

not occur. Weak turbulence and weak mixing can be seen from Figs. 5a and 5b so that the modifications in EXP5 prevent the system from decoupling. It is particularly noteworthy in Figs. 5a and 5b how effective *the small but nonzero* nighttime turbulent mixing is at maintaining effective nighttime coupling during day 2 and day 3 in the CTL. A comparison of temperature profiles at Albany (shown in Fig. 4c) at 1200 UTC 18 February shows that the T_{2m} (254.0 K) in EXP5 is close to observed (252.6 K), and the warm bias at the lowest model level and three model levels above in CTL is clearly reduced in EXP5 owing to the proper downward heat transport between the land and the atmosphere in very stable surface layer conditions. Figure 4c also shows that both CTL and EXP5 tend to produce cold biases in parts of the lower tropsophere, which is mostly associated with the treatment of vertical turbulence mixing under stable conditions in the planetary boundary layer scheme. Based on the studies of Han and Pan (2011) and Han et al. (2016), too strong vertical turbulent mixing results in a too deep stable layer, while too weak vertical turbulent mixing can produce cold and moist biases in the lower troposphere during the nighttime. As shown in Fig. 4d, the observed wind profile displays quite weak wind below 200-m height and almost zero vertical wind shear from 300- to 900-m height, indicating that there exists a very large local gradient Richardson number and strongly stable boundary layer. Both CTL and EXP5 fail to produce very weak wind speed or very weak vertical wind shear and consequently show biases of wind speed of 1–2 $m\,s^{-1}$.

It is also noted in Fig. 5c that the observed wind speed shows intermittency at a fixed station point during the evening of 17 or 18 February, but the model does not. This intermittency will occur not only in time but also spatially within the nearby area. Since the model result represents a grid box and not a single point, such intermittency across the gridbox area in the real world implies the areal average turbulence.

The latter point is vividly illustrated in Fig. 6 by comparing the early nighttime surface *sensible heat flux* of the CTL versus EXP5 at the Utica location. As evident from Fig. 6, the latent heat flux and ground heat flux do not exhibit much difference between these two runs, and during the nighttime there is almost no latent heat flux, as expected. The net radiation shows some difference during the nighttime, mainly from a difference in the upward longwave radiation (not shown). The obvious difference is found in the friction velocity and sensible heat flux. More specifically, in the late afternoon on 16 February as the winds become weak, the turbulence u_* in CTL approaches zero, and the sensible heat flux also vanishes. Under this condition of virtually zero

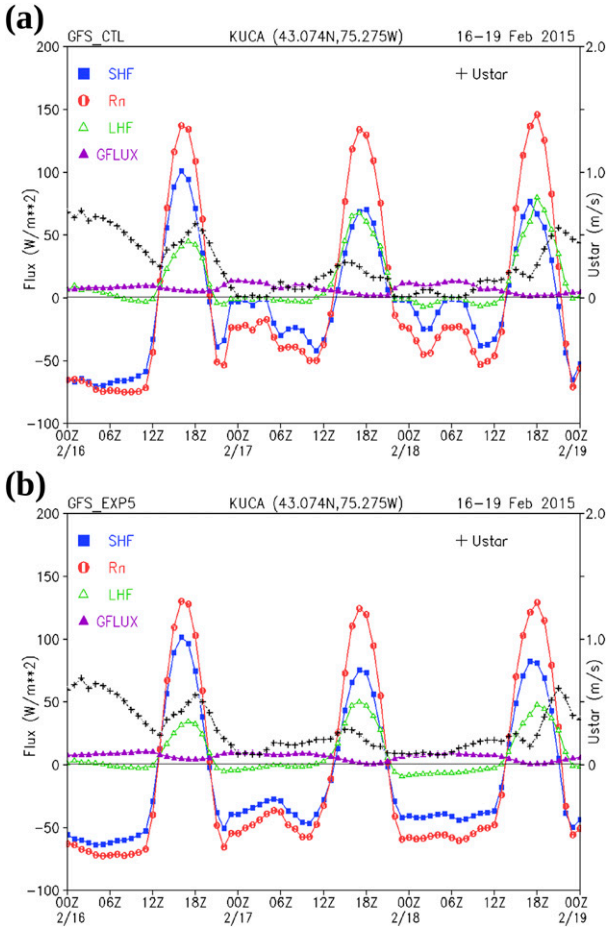

FIG. 6. Hourly time series at Utica, NY, for (a) CTL and (b) EXP5 for surface sensible heat flux (blue; W m^{-2}), latent heat flux (green; W m^{-2}), ground heat flux (purple; W m^{-2}), net radiation (red; W m^{-2}), and friction velocity (black; m s^{-1}) during the 72-h period in Fig. 3.

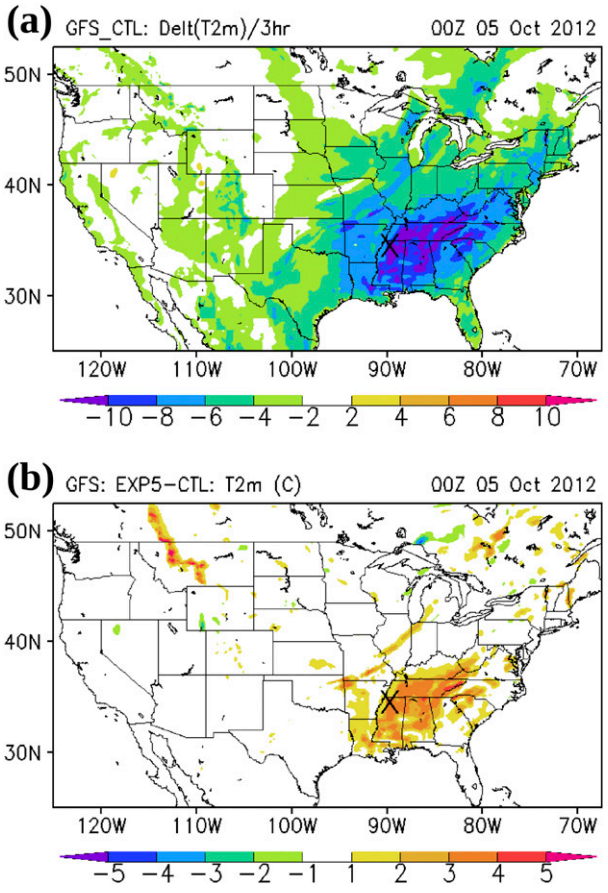

FIG. 7. The 3-h change in GFS forecast of T_{2m} (°C) in (a) CTL from 2100 UTC 4 Oct to 0000 UTC 5 Oct 2012 and (b) difference of 2-m temperature (°C) between EXP5 and CTL at 0000 UTC 5 Oct 2012. The "X" denotes the location of Goodwin Creek, MS.

turbulence, the surface energy budget includes only the net radiation and ground heat flux. Similar behavior is evident in the late afternoon on 17 February. The turbulence stops until 0000 UTC 18 February, and then weak turbulence emerges but disappears again after a few hours, which indicates the intermittent turbulence behavior in the CTL configuration.

By introducing the constraint on the MO stability parameter via the limiting value in Eq. (1) on the stability parameter z/L, the cessation of turbulence does not happen in EXP5. Rather, weak but nonzero turbulence is maintained, which sustains weak but nonzero sensible heat flux in the late afternoon and nighttime. A minor adverse effect of this new approach evident in Fig. 3 is that the small negative sensible heat flux during the nighttime and early morning appears to produce a modest warm bias of 2-m temperature during later nighttime and early morning.

b. *Autumn snow-free case*

For a second case of extremely rapid drop in surface temperatures, we selected a snow-free area with no clouds or fog in autumn in the southeastern United States. During the period from 2 to 6 October 2012, a weak surface high pressure system dominated the region from the Mississippi Valley to the Southeast, and consequently the surface winds became quite weak.

Similar to the above case over snowpack, GFS 7-day forecasts were executed for a control run and five sensitivity experiments initiated at 0000 UTC 2 October 2012. In the GFS control run, overly rapid cooling again happens in some regions in the late afternoon on 2 and 4 October. Figure 7a presents the 2-m temperature change for the 3-h period ending at 0000 UTC 5 October 2012. An unreasonably rapid and large drop in 2-m temperature is evident over the Southeast, showing a change of more than 10°C in some areas therein. As shown in Fig. 7b, the EXP5 run again reduces the large

temperature drop by about half in those areas manifesting the biggest drop in CTL.

The Surface Radiation Budget Network (SURFRAD) (Augustine et al. 2000) station at Goodwin Creek, Mississippi, is located within the rapid cooling region cited above. This station is covered by deciduous broadleaf forecast, and the z_{0M} is 0.826 m in CTL, EXP3, and EXP4, and 0.5 m in EXP1, EXP2, and EXP5. Thus, the GFS forecasts can be assessed against the SURFRAD observations at this station such as 2-m temperature, surface skin temperature, and radiation fluxes. Figure 8a shows a comparison of the hourly time series of observed and GFS forecast 2-m temperature (control and the five experiments) at Goodwin Creek during the 4-day period from 0000 UTC 2 October to 6 October 2012. The overly rapid drop in GFS 2-m temperature occurs in late afternoon on 2 and 4 October in all GFS runs except for EXP4 and EXP5. Compared to the observations on these two days, both EXP4 and EXP5 show a reasonable 2-m temperature forecast, while the other experiments yield a large cold bias before and after sunset, as in CTL.

The surface skin temperature verification can be found in Fig. 8b, and its variations are similar to the 2-m air temperature. Around sunset, the EXP4 and EXP5 runs are quite close to the observations, but EXP4 exhibits a somewhat warmer bias than EXP5 during a period from 0000 to 1200 UTC 5 October because of a higher z_{0M} value and stronger constraint of the MO stability parameter at this station in EXP4, while the other experiments show a cold bias analogous to that in the 2-m air temperature. However, the daytime skin temperatures in all the GFS runs, including EXP4 and EXP5, exhibit a cold bias compared to the observations during the first two days. Of course, daytime hours in the autumn in the southeastern United States are not typically the time of day for a stable surface layer, which is the stability regime targeted by EXP4 or EXP5. However, the updated z_{0M} test (EXP2) and the increase of C_{zil} test (EXP3) do give some hint of reduced daytime cold bias, and the combination of these two changes (EXP1or EXP5) indicates some modest further improvement in Fig. 8 in the daytime cold bias of the forecast of skin temperature.

Weak surface winds are closely associated with the overly rapid cooling of the 2-m temperature, as shown in Fig. 8c. The observed surface winds are relatively large during the daytime but decrease very rapidly in the late afternoon. In particular, they become almost calm during a period from 0000 to 1200 UTC 3–5 October. All five experiments fail to reproduce the very weak nighttime surface winds, yielding a high bias in nighttime wind speed. EXP4 and EXP5 show some reduction of

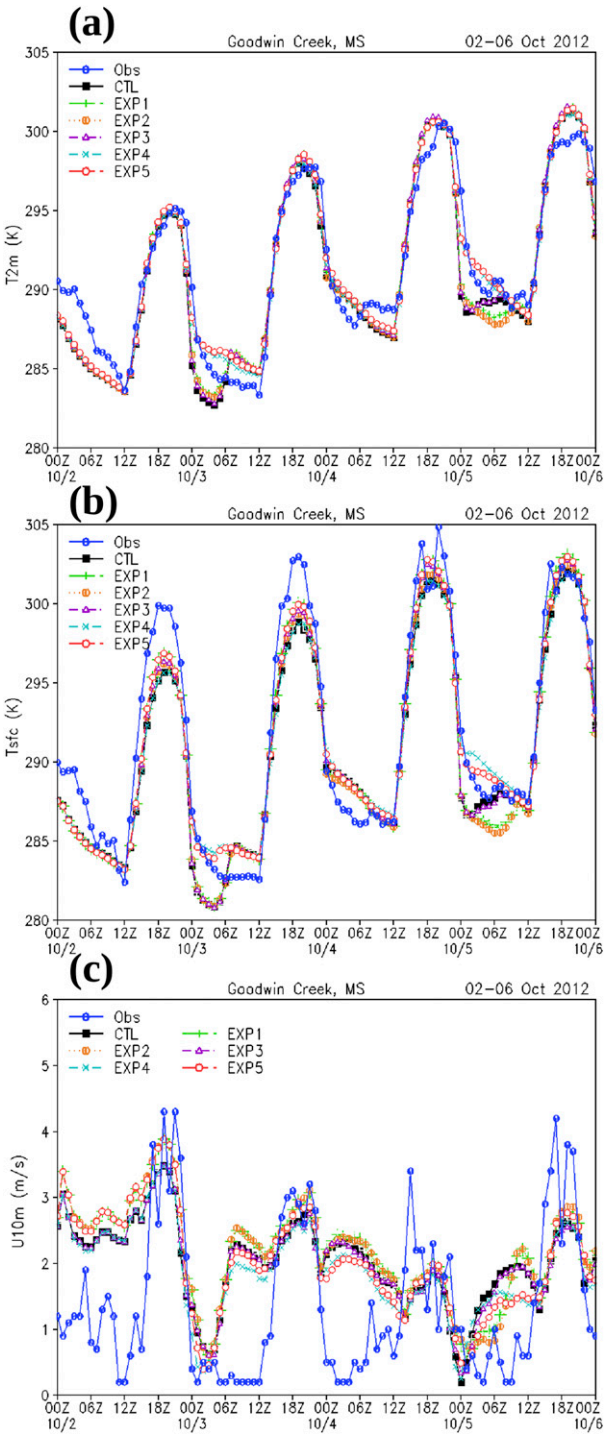

FIG. 8. Hourly time series at the SURFRAD site of Goodwin Creek, MS (at location of X in Fig. 7), for (a) T_{2m} (K), (b) T_{skin} (K), and (c) surface wind speed (m s^{-1}) during the 96-h period from 0000 UTC 2 Oct to 0000 UTC 6 Oct 2012 for observations (blue), CTL (black), EXP1 (green), EXP2 (orange), EXP3 (purple), EXP4 (light blue), and EXP5 (red).

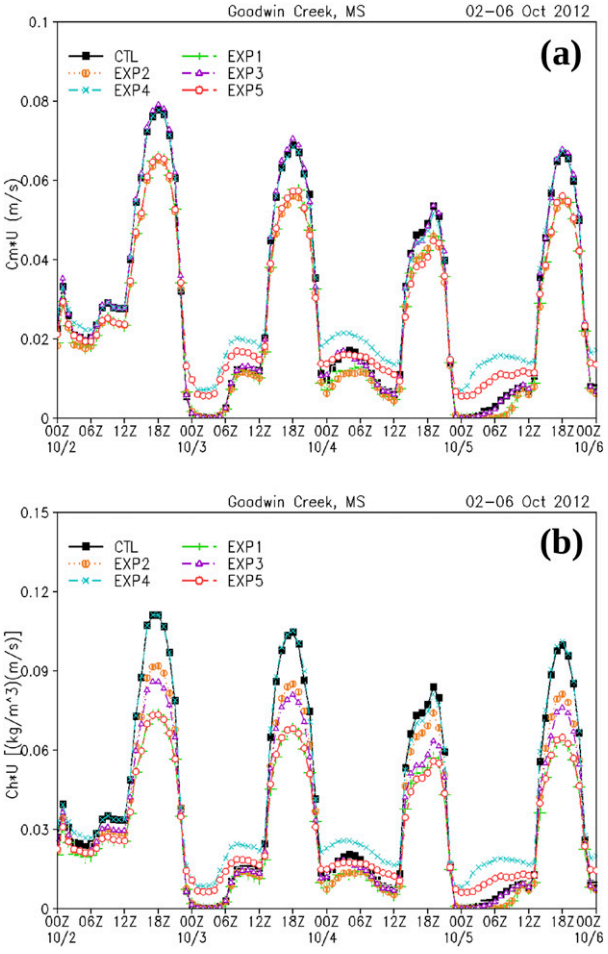

FIG. 9. Hourly time series at Goodwin Creek, MS, for surface aerodynamic conductance for (a) momentum ($m\,s^{-1}$) and (b) heat ($kg\,m^{-3}\,m\,s^{-1}$) for CTL (black), EXP1 (green), EXP2 (orange), EXP3 (purple), EXP4 (light blue), and EXP5 (red) during the 96-h period in Fig. 8.

the high bias. Figures 8a and 8b show the model does not exhibit rapid cooling on 4 October but does show a little warm bias because of the higher surface winds.

The surface aerodynamic conductance represents the intensity of the near-surface vertical turbulence that vertically transports momentum, heat, and moisture, and thus is considered an important parameter for determining the land–atmospheric coupling "strength." Given that the aerodynamic conductance is not observed, Figs. 9a and 9b present only comparisons of GFS simulated aerodynamic conductance for momentum C_MU and aerodynamic conductance for heat and moisture C_HU. Except for EXP4 and EXP5, all other GFS runs show the aerodynamic conductance for momentum, or for heat and moisture, approaches zero around 0000 UTC 3 and 5 October. However, in EXP4 or EXP5, while the aerodynamic conductance also decreases rapidly in the late afternoon, it does not approach zero and therefore weak turbulence is sustained during the late afternoon and nighttime periods. It is noted that because of higher value of the momentum roughness length z_{0M} at this station, the aerodynamic conductance for momentum, or for heat and moisture, in EXP4 is larger than that in EXP5, indicating EXP4 sustains more turbulence under very stable conditions, which results in a warmer bias of the surface skin temperature as shown in Fig. 8b.

Turning our attention briefly to the daytime period, Fig. 9 also shows that the proposed alternative approach to the momentum roughness length z_{0M} in EXP2 alters the daytime aerodynamic conductance for momentum. For the daytime aerodynamic conductance for heat and moisture, both the alternative z_{0M} (EXP2) and alternative C_{zil} (EXP3) approaches reduce it, thus resulting in less surface heat and moisture flux during the daytime and improvement of the daytime surface skin temperature (as shown in Fig. 8b). With small C_{zil} like CTL, EXP4 has high z_{0H} and large aerodynamic conductance for heat, resulting in a large cold bias of the daytime surface skin temperature, which is notably reduced in EXP5.

5. Assessment of daily winter forecast tests

To further examine the impact of the new stable surface layer approach we propose for the GFS, daily GFS forecasts are carried out for a winter period exceeding 40 days spanning 21 January to 2 March 2015. During this season, many users of the operational GFS forecast products and the Model Evaluation Group in the EMC of NCEP had reported numerous instances of excessive cooling of 2-m air temperature forecasts over land in the late afternoon and nighttime. The CTL uses the current operational GFS version. The EXP in this section includes all three model changes summarized at the beginning of section 4 (i.e., all the changes included in the experiment denoted EXP5 in section 4). Both the CTL and EXP versions of the GFS are executed for 7-day forecasts initialized at 0000 UTC each day of the period described above.

The model outputs are compared to the validating surface and vertical sounding observations by means of the NCEP/EMC Global NWP Model Deterministic Forecast Verification Package. This package provides verification statistics for the 14 subregions of CONUS depicted in Fig. 10, and for larger CONUS regions defined as combinations of 2 or more of the 14 subregions, such as the 6 subregions defined by the union of the labeled regions denoted by red circles in Fig. 10. Also, the Alaskan subregion is shown in the inset of Fig. 10. Finally, we will show model verification results for two very large CONUS subregions that altogether include

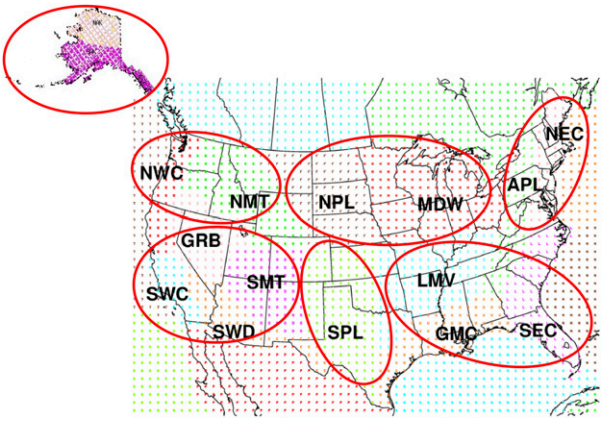

FIG. 10. The seven subregions (denoted by red circles) over CONUS that were utilized in the NCEP/EMC Global NWP Model Deterministic Forecast Verification Package.

all 14 subregions as follows: 1) a substantially semiarid "west CONUS" region that includes northern West Coast (NWC), southern West Coast (SWC), Great Basin (GRB), northern mountain (NMT), southern mountain (SMT), southwest desert (SWD), northern plains (NPL), and southern plains (SPL); and 2) an "east CONUS" region, mostly covered by forests and crops, and spanning the subregions of Midwest (MDW), Appalachians (APL), lower Mississippi Valley (LMV), Gulf of Mexico coast (GMC), southern East Coast (SEC), and northern East Coast (NEC).

In the winter season, persistent snow cover typically exists over the western and northern reaches of the CONUS, thus increasing the likelihood of the occurrence of very stable boundary layers. Figures 11 presents the areal and temporal mean diurnal cycle (Fig. 11a) and root-mean-square error (RMSE) (Fig. 11b) of the CTL and EXP GFS forecasts of 2-m surface air temperature over east CONUS, as a function of the model 7-day forecast length. Compared to observations, both CTL and EXP exhibit a mostly cold bias during daytime and nighttime, but the EXP reduces the cold bias in the late afternoon and early nighttime up to 0.3°C. The reduction of RMSE is quite obvious during the 7-day forecast, particularly around 0000 UTC each day, which for east CONUS is a transitional period from daytime unstable conditions to nocturnal stable conditions. The impacts depicted in Fig. 11 from the GFS surface layer scheme changes are admittedly small, but larger impacts are seen in later figures below for colder regions, because the significant impacts from the proposed changes to the surface layer occur only episodically in situations of a very stable boundary layer, as illustrated for specific instances and situations in section 4. In these latter specific instances, section 4 shows that the improvements from

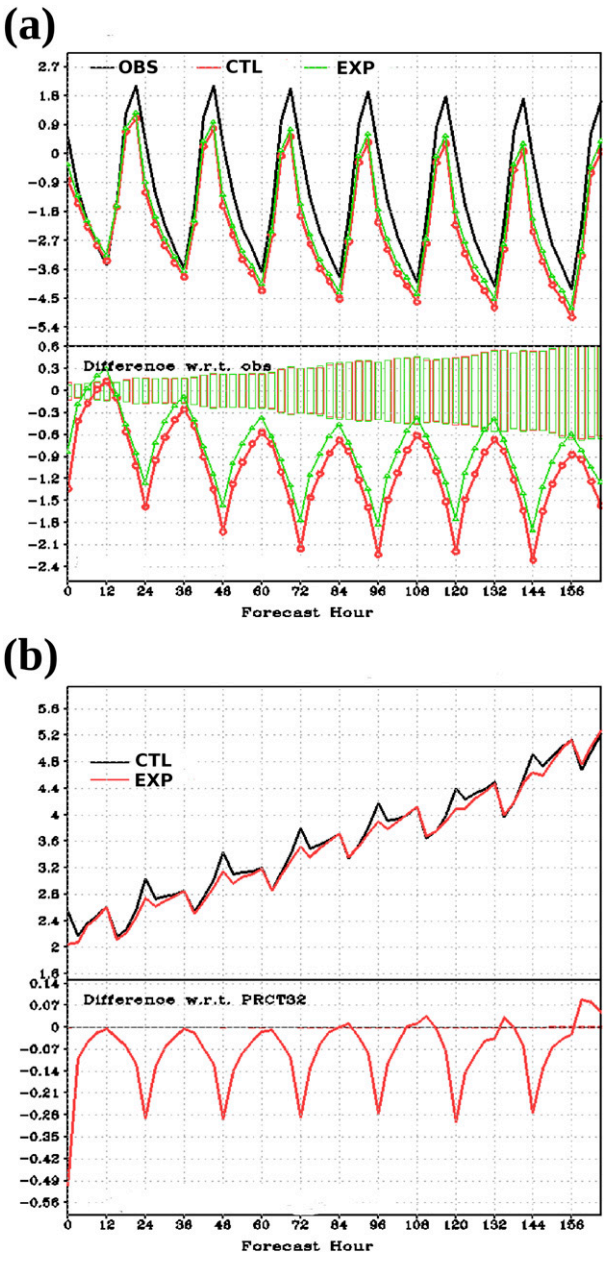

FIG. 11. (a) (top) Mean 7-day diurnal cycle of T_{2m} (°C) averaged both spatially over the east CONUS region (see Fig. 10) and temporally over the winter period of 21 Jan–2 Mar 2015, for observations (black), and 7-day GFS forecast from CTL (red) and EXP (green); (bottom) as in (top), but shows difference of CTL (red) and EXP (green) from observations, plus the results of a statistical Student's t test/significance test. The differences outside of the hollow bars attain the 95% confidence level based on the Student's t tests. (b) (top) Corresponding RMSE of CTL (black) and EXP (red) with respect to observations as function of forecast length over 7 days for the same period as in (a); (bottom) difference of CTL and EXP time series in the top plot, plus the results of a statistical Student's t test/significance test. The differences outside of the hollow bars attain the 95% confidence level based on the Student's t tests.

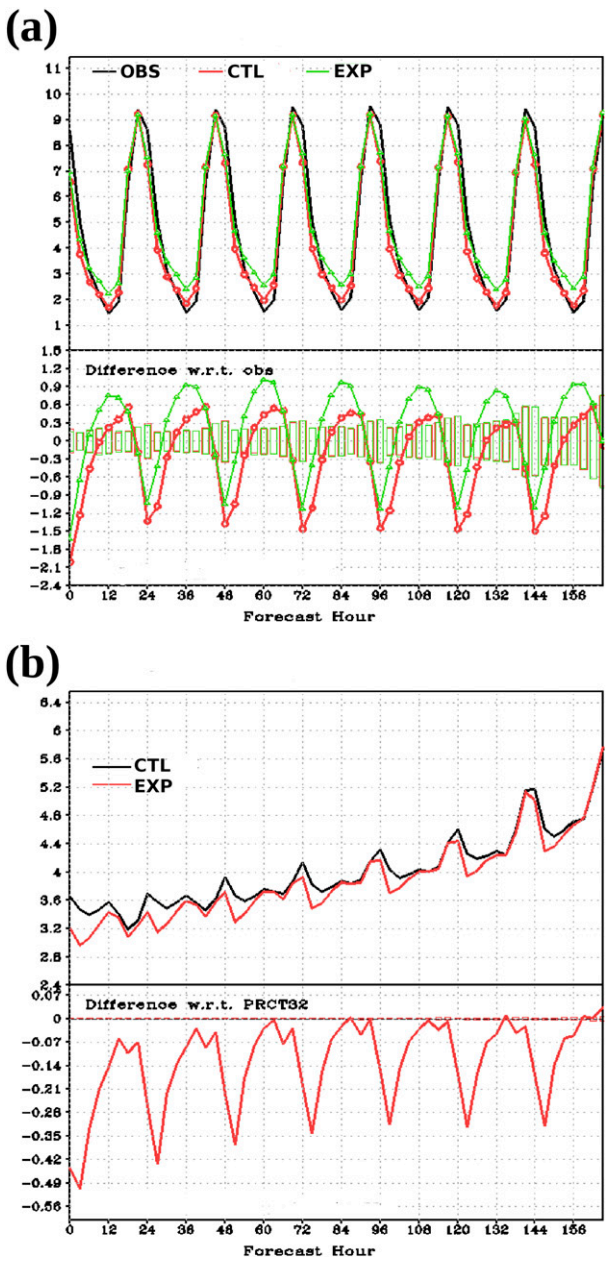

FIG. 12. As in Fig. 11, but for west CONUS.

the proposed changes are very large and beneficial. *The focus here in this section is on a span of over 40 days of daily GFS winter forecasts to demonstrate that the changes slightly improve or do not materially degrade the overall GFS forecast accuracy throughout an entire month or more of model forecasts over major regions of the United States.*

Over west CONUS, the CTL exhibits a modest warm bias during the nighttime but otherwise exhibits 2-m temperatures lower than the observations, with the cold bias reaching 1.5°C in the late afternoon (Figs. 12a and 12b). The EXP reduces the late afternoon cold bias but adds modestly more nighttime warm bias. However, the RMSE shows quite consistent reduction in the EXP versus the CTL, especially near sunset. The nighttime warm bias of west CONUS is contributed mostly by the southwest subregions including SWC, SMT, SWD, and GRB, where bare soil or sparse broadleaf shrub is the vegetation type. The other subregions also show the model changes have a positive impact on the surface temperature forecast, except for the SPL subregion, which shows a neutral impact.

The substantial improvement of the 2-m temperature forecast can be seen more clearly in the northerly subregions such as Alaska, the Northwest, and the Northeast. Figure 13a presents the 2-m temperature changes in the Northwest subregion, which is mostly covered by needleleaf evergreen forest, which is characterized by large roughness length. The late afternoon and nighttime 2-m temperature in the CTL exhibits temperatures up to 3°C lower than the observations, and the EXP significantly reduces this cold bias, with reductions up to 1.2°C near sunset. The RMSE in the CTL indicates large errors in the late afternoon (Fig. 13b). The reduction of RMSE in the EXP is evident and reaches as large as 1°C, which amounts to about a 25% reduction of total RMSE versus the CTL. It is noteworthy that the daytime RMSE also dropped in the EXP.

As discussed in section 4, the excessive surface cooling and associated decoupling that arises from the very small, or virtually zero, surface sensible heat flux can result in a counterpart *warm* bias in the lower atmosphere *above* the surface layer. Figure 14 presents the bias and RMSE of vertical temperature profiles of the CTL and EXP runs verified against radiosonde observations in the Northern Hemisphere (from 20° to 80°N) and in the North America region (from 25° to 60°N and from 145° to 50°W) at the 12- and 36-h forecast lengths. The CTL exhibits warm biases in the lower troposphere in the Northern Hemisphere, including the North American region. The reduction of the lower-tropospheric warm bias in the EXP is apparent, and the RMSE also exhibits a reduction in the EXP in the lower troposphere, both for 12- and 36-h forecasts. Negligible improvement or no negative impact from the proposed modifications is noted in the Southern Hemisphere (from 20° to 80°S) and tropical regions (from 20°S to 20°N) (not shown). The spatial and temporal extent of very stable surface layers is of course much less in the tropics and Southern Hemisphere during Northern Hemisphere winter.

Verification of the GFS precipitation forecast over CONUS against ground-based precipitation observations for the 12–84-h forecast range indicates positive impact from the model changes. In Fig. 15, the Model

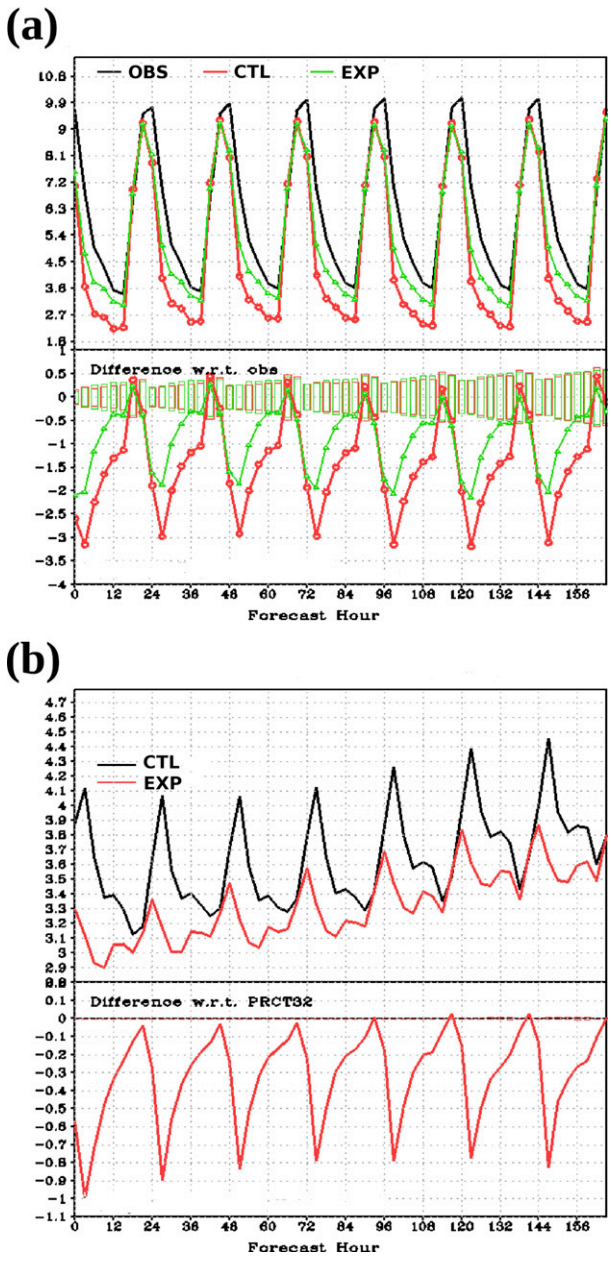

FIG. 13. As in Fig. 11, but for northwest CONUS.

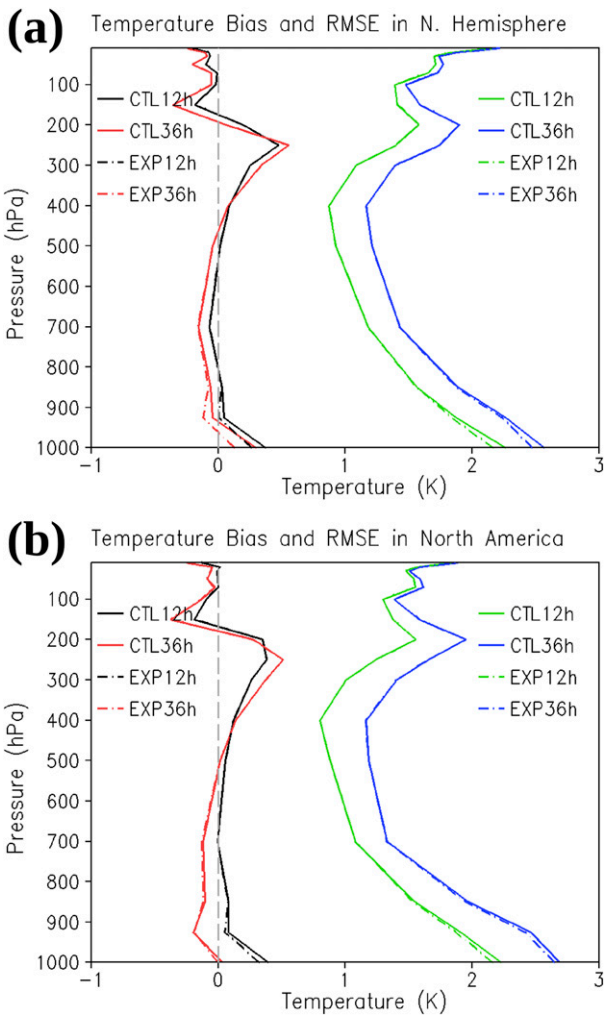

FIG. 14. Mean vertical profiles of air temperature (K) bias and RMSE for CTL (solid) and EXP (dot–dash) forecasts verified against radiosonde observations, as temporally averaged over the winter period of 21 Jan–2 Mar 2015 and spatially averaged over the (a) Northern Hemisphere and (b) North America. Black lines (red lines) are bias from 12-h (36 h) forecasts. Green lines (blue lines) are RMSE from 12-h (36 h) forecasts.

Deterministic Forecast Verification Package applies the Monte Carlo significance test rather than the Student's *t* test applied in Figs. 11–13 because the conventional method of significance tests such as the Student's *t* test is not applicable for precipitation skill scores. As shown in Fig. 15 for skill scores of the GFS precipitation forecast over CONUS during the 60–84-h forecast range, the EXP yields higher equitable threat scores than the CTL, and this skill difference attains the 95% confidence level for the majority of the light and medium precipitation amounts. Bias reduction in EXP versus CTL is quite consistent from light to heavy precipitation and significant at the 95% confidence level for light and medium precipitation. Therefore, the improvement of land–atmosphere interaction processes in the model can reduce errors of surface temperature and errors of the vertical temperature profiles, modify the boundary layer structure and atmospheric stability, and finally have a significant impact on the precipitation processes.

6. Conclusions

The NCEP GFS global prediction model has experienced a longstanding problem of severe cold bias

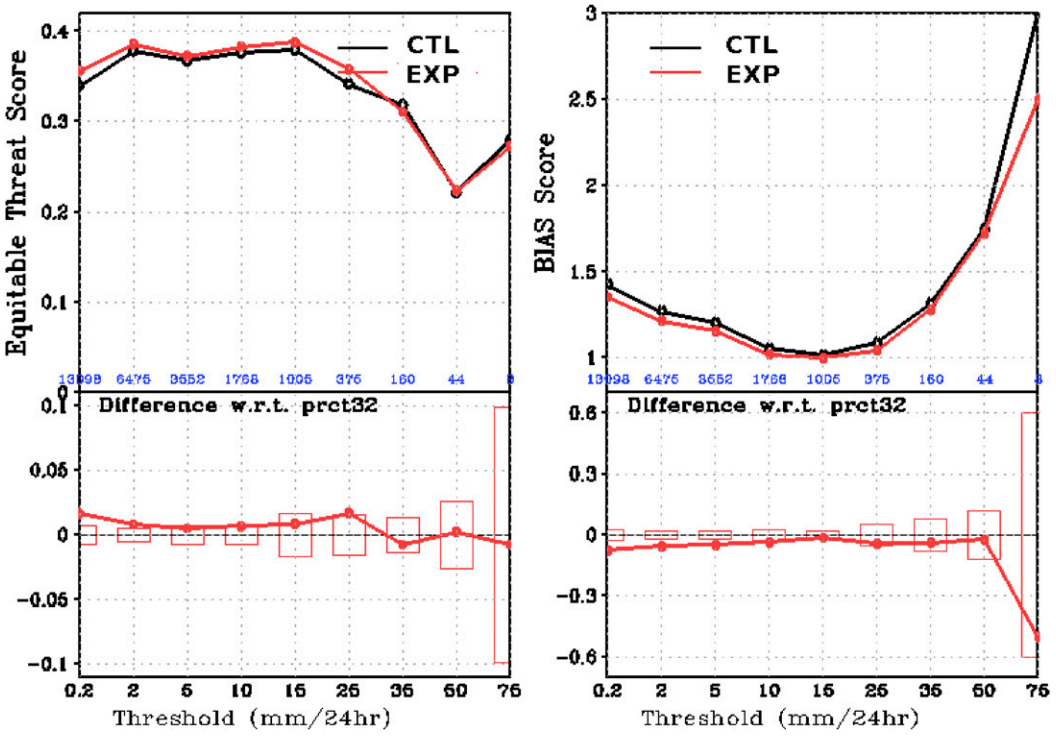

FIG. 15. (left) Precipitation equitable threat scores and (right) bias scores of the GFS precipitation forecast over CONUS for the CTL (black) and the EXP (red), as temporally averaged over the winter period of 21 Jan–2 Mar 2015. The blue numbers in the top plots denote number of observation stations, and bottom panels indicate their differences with the Monte Carlo significance tests. The differences outside of the hollow bars attain the 95% confidence level based on 10 000 Monte Carlo tests.

in the 2-m air temperature forecasts over land in the late afternoon and nighttime during most seasons. This cold bias is closely associated with the nocturnal stable boundary layer (and is accompanied by a corresponding warm air temperature bias in the first model level above the ground). This study identified the cause of the large surface cold bias by examining the GFS surface layer parameterization and proposing and testing practical approaches to reduce the bias.

GFS experiments in both a winter case with snowpack and a snow-free autumn case demonstrated that three proposed GFS modifications 1) considerably reduce the excessive cooling of surface skin temperature and 2-m air temperature and 2) prevent the collapse of turbulence and potential numerical instability resulting from thermal decoupling of the land surface and atmosphere. The most effective of the three modifications is the introduction of a limiting condition, following Van de Wiel et al. (2007), on the z/L stability parameter in the Monin–Obukov similarity theory, with implication that the model is only able to capture the near-neutral to weakly stable regime. The warm temperature bias at the first model layer was also reduced by this modification, which yielded a more proper downward heat transport between the land and the atmosphere in very stable surface layer conditions. Last, the other two modifications, which involved alternative formulations of 1) the momentum roughness length and 2) the so-called C_{zil} parameter applied in the thermal roughness length calculation, altered the GFS daytime aerodynamic conductance and thereby improved the GFS daytime forecast of land surface skin temperature.

A comprehensive set of daily GFS 7-day forecast experiments spanning more than one month in winter demonstrated that using the proposed three approaches considerably reduced the 2-m temperature cold bias and RMSE in the late afternoon and early nighttime. Moreover, because of the improvement of the interaction of the land and the atmosphere, these model changes impacted model levels above the surface layer and reduced the bias and RMSE of atmospheric temperatures in the lower troposphere. Last, the results also revealed that the improvements of the near-surface temperature and the low-level temperature, and the attendant influence on the large-scale flow arising from the model changes, yield generally positive impacts on the skill of GFS forecasts of light and medium precipitation amounts over the CONUS.

As mentioned before, the proposed approach focuses on a proper treatment of surface layer parameterization under very stable conditions in the NCEP GFS to prevent excessive cooling of 2-m surface air temperature forecasts and decoupling between the surface and the atmosphere. It is fair to point out that although the results indicate these changes bring about considerable improvement in forecasts of 2-m surface air temperature and vertical temperature profiles, as well as improved precipitation forecast skill over most regions, some regions such as those dominated by bare soil exhibit a slightly higher warm bias with the proposed model changes. However, the warm bias increase is quite small. In the future, new land datasets such as new fields of vegetation and soil type, near-real-time green vegetation fraction, and land surface albedo will be updated in the GFS and further reduction of model forecast errors is anticipated.

Acknowledgments. The authors thank Glenn White and Geoffrey Manikin from NCEP/EMC Model Evaluation Group for the cases' selection. The authors also highly appreciate many suggestions and beneficial comments from Mark Iredell, Shrinivas Moorthi, Jongil Han, Ruiyu Sun, Fanglin Yang, Ying Lin, and Vijay Tallapragada at NCEP/EMC. Internal reviews from Ruiyu Sun and Youlong Xia at NCEP Environmental Modeling Center are acknowledged. Anonymous reviewers are thanked for the constructive comments and suggestions. This work was completed at NOAA/NCEP/Environmental Modeling Center.

APPENDIX

The Stable Surface Layer Parameterization Scheme in the GFS

To help to understand the stable surface layer parameterization scheme in the GFS (Long 1986), some pertinent features are described below.

In a numerical model, the turbulent fluxes of momentum τ, heat SH, and moisture LH in the surface layer for both unstable and stable conditions are given by

$$\tau = -\rho C_M U_a^2, \tag{A1}$$

$$\mathrm{SH} = -\rho C_p C_H U_a(\theta_a - \theta_s), \quad \text{and} \tag{A2}$$

$$\mathrm{LH} = -\rho L_v C_H U_a(q_a - q_s), \tag{A3}$$

where U_a, θ_a, and q_a are the absolute wind speed, potential temperature, and specific humidity, respectively, at height of the first model level; θ_s is the surface potential temperature; q_s is the surface specific humidity; C_p is the specific heat of air; L_v is the latent heat of vaporization; and ρ is the air density. The bulk transfer coefficients for momentum C_M and heat C_H can be expressed as

$$C_M = k^2/F_M^2 \quad \text{and} \tag{A4}$$

$$C_H = k^2/F_M F_H, \tag{A5}$$

where k is the von Kármán constant, and $F_{M,H}$ are obtained by integrating the vertical profile stability functions $\varphi_{M,H}$ according to

$$F_{M,H} = \int_{z_{0M,H}}^{z} \frac{dz'}{z'} \varphi_{M,H}(z'/L), \tag{A6}$$

in which z is the height above the surface; $z_{0M,H}$ denotes momentum and thermal roughness lengths, respectively; and $z > z_{0M,H}$. The vertical profile stability functions $\varphi_{M,H}$ are defined with the friction velocity u_* and the temperature scaling θ_* as

$$\varphi_M\left(\frac{z}{L}\right) = \frac{kz}{u_*}\frac{\partial U}{\partial z} \quad \text{and} \tag{A7}$$

$$\varphi_H\left(\frac{z}{L}\right) = \frac{kz}{\theta_*}\frac{\partial \theta}{\partial z}. \tag{A8}$$

The functions $\varphi_{M,H}$ are the universal nondimensional vertical shears of wind speed U and potential temperature θ. The Obukhov length L in Eq. (A6) is defined by

$$L = \frac{\theta}{kg}\frac{u_*^2}{\theta_*}, \tag{A9}$$

where g is the gravitational constant.

For stable conditions, unlike the standard form found in MO similarity in terms of z/L, the form of $\varphi_{M,H}$ is specified by

$$\varphi_M = \varphi_H = (1 + \alpha R), \tag{A10}$$

where α is a constant parameter and $\alpha = 5$ is typically used (Dyer 1974), $R = (g/\theta)(\partial\theta/\partial z)(\partial U/\partial z)^{-2}$, which is known as the gradient Richardson number. The MO stability parameter $\xi = z/L$ can be obtained as

$$\xi = \frac{\varphi_M^2}{\varphi_H} R. \tag{A11}$$

Applying Eq. (A11), Eq. (A10) becomes

$$\varphi_M = \varphi_H = \frac{1}{2}(1 + \sqrt{1 + 4\alpha\xi}). \tag{A12}$$

Finally, after performing the integration in Eq. (A6) using Eq. (A12), one obtains

$$F_{M,H} = \ln\frac{z}{z_{0M,H}} - \psi_{M,H}\left(\frac{z}{L};\frac{z_{0M,H}}{L}\right), \qquad \text{(A13)}$$

where

$$\psi_{M,H} = \sqrt{1+4\alpha\xi_{0M,H}} - \sqrt{1+4\alpha\xi} + \ln\frac{\sqrt{1+4\alpha\xi}+1}{\sqrt{1+4\alpha\xi_{0M,H}}+1}, \qquad \text{(A14)}$$

and $\xi_{0M,H} = z_{0M,H}/L$.

REFERENCES

Atlaskin, E., and T. Vihma, 2012: Evaluation of NWP results for wintertime nocturnal boundary-layer temperatures over Europe and Finland. *Quart. J. Roy. Meteor. Soc.*, **138**, 1440–1451, doi:10.1002/qj.1885.

Augustine, J. A., J. J. DeLuisi, and C. N. Long, 2000: SURFRAD—A national surface radiation budget network for atmospheric research. *Bull. Amer. Meteor. Soc.*, **81**, 2341–2357, doi:10.1175/1520-0477(2000)081<2341:SANSRB>2.3.CO;2.

Basu, S., A. A. M. Holtslag, B. J. H. van de Wiel, A. F. Moene, and G. J. Steeneveld, 2008: An inconvenient "truth" about using sensible heat flux as a surface boundary condition in models under stably stratifeid regimes. *Acta Geophys.*, **56**, 88–99, doi:10.2478/s11600-007-0038-y.

Bosveld, F. C., and Coauthors, 2014: The third GABLS intercomparison case for evaluation studies of boundary-layer models. Part B: Results and process understanding. *Bound.-Layer Meteor.*, **152**, 157–187, doi:10.1007/s10546-014-9919-1.

Brutsaert, W., 1975: The roughness length for water vapor, sensible heat, and other scalars. *J. Atmos. Sci.*, **32**, 2028–2031, doi:10.1175/1520-0469(1975)032<2029:TRLFWV>2.0.CO;2.

Chen, F., and Y. Zhang, 2009: On the coupling strength between the land surface and the atmosphere: From viewpoint of surface exchange coefficients. *Geophys. Res. Lett.*, **36**, L10404, doi:10.1029/2009GL037980.

Couvreux, F., E. Bazile, G. Canut, Y. Seity, M. Lothon, F. Lohou, F. Guichard, and E. Nilsson, 2016: Boundary-layer turbulent processes and mesoscale variability represented by numerical weather prediction models during the BLLAST campaign. *Atmos. Chem. Phys.*, **16**, 8983–9002, doi:10.5194/acp-16-8983-2016.

Derbyshire, S. H., 1999: Boundary-layer decoupling over cold surface as a physical boundary instability. *Bound.-Layer Meteor.*, **90**, 297–325, doi:10.1023/A:1001710014316.

Dirmeyer, P. A., and Coauthors, 2012: Evidence for enhanced land–atmosphere feedback in a warming climate. *J. Hydrometeor.*, **13**, 981–995, doi:10.1175/JHM-D-11-0104.1.

Dyer, A. J., 1974: A review of flux-profile relationships. *Bound.-Layer Meteor.*, **7**, 363–372, doi:10.1007/BF00240838.

Ek, M. B., 2004: *Interactions of the Land-Surface with the Atmospheric Boundary Layer*. Ponsen & Looijen, 210 pp.

——, K. E. Mitchell, Y. Lin, E. Rogers, P. Grunmann, V. Koren, G. Gayno, and J. D. Tarpley, 2003: Implementation of Noah land-surface model advances in the NCEP operational mesoscale Eta model. *J. Geophys. Res.*, **108**, 8851, doi:10.1029/2002JD003296.

Fernando, H. J. S., and J. C. Weil, 2010: Whither the stable boundary layer? *Bull. Amer. Meteor. Soc.*, **91**, 1475–1484, doi:10.1175/2010BAMS2770.1.

Freedman, F. R., and M. Ek, 2004: Testing NCEP operational surface layer parameterizations for stable conditions using CASES99 data. *16th Symp. on Boundary Layers and Turbulence*, Portland, ME, Amer. Meteor. Soc. [Available online at https://ams.confex.com/ams/BLTAIRSE/webprogram/Paper78457.html.]

Gibbs, J. A., E. Fedorovich, and A. Shapiro, 2015: Revisiting surface heat-flux and temperature boundary conditions in models of stably stratified boundary-layer flows. *Bound.-Layer Meteor.*, **154**, 171–184, doi:10.1007/s10546-014-9970-y.

Grachev, A. A., E. L Andreas, C. W. Fairall, P. S. Guest, and P. O. G. Persson, 2013: The critical Richardson number and limits of applicability of local similarity theory in the stable boundary layer. *Bound.-Layer Meteor.*, **147**, 51–82, doi:10.1007/s10546-012-9771-0.

——, ——, ——, ——, and ——, 2015: Similarity theory based on the Dougherty–Ozmidov length scale. *Quart. J. Roy. Meteor. Soc.*, **141**, 1845–1856, doi:10.1002/qj.2488.

Hagemann, S., 2002: An improved land surface parameter dataset for global and regional climate models. Rep. 336. [Available online at http://hdl.handle.net/11858/00-001M-0000-0012-02A3-9.]

Han, J., and H.-L. Pan, 2011: Revision of convection and vertical diffusion schemes in the NCEP Global Forecast System. *Wea. Forecasting*, **26**, 520–533, doi:10.1175/WAF-D-10-05038.1.

——, M. L. Witek, J. Teixeira, R. Sun, H.-L. Pan, J. K. Fletcher, and C. S. Bretherton, 2016: Implementation in the NCEP GFS of a hybrid eddy-diffusivity mass-flux (EDMF) boundary layer parameterization with dissipative heating and modified stable boundary layer mixing. *Wea. Forecasting*, **31**, 341–352, doi:10.1175/WAF-D-15-0053.1.

Holtslag, A. A. M., G. J. Steeneveld, and B. J. H. van de Wiel, 2007: Role of land-surface temperature feedback on model performance for the stable boundary layer. *Bound.-Layer Meteor.*, **125**, 361–376, doi:10.1007/s10546-007-9214-5.

——, and Coauthors, 2013: Stable atmospheric boundary layers and diurnal cycles: Challenges for weather and climate models. *Bull. Amer. Meteor. Soc.*, **94**, 1691–1706, doi:10.1175/BAMS-D-11-00187.1.

Hong, S.-Y., and H.-L. Pan, 1996: Nonlocal boundary layer vertical diffusion in a medium-range forecast model. *Mon. Wea. Rev.*, **124**, 2322–2339, doi:10.1175/1520-0493(1996)124<2322:NBLVDI>2.0.CO;2.

Long, P. J., 1984: An general unified similarity theory for the calculation of turbulent fluxes in the numercal weather prediction models for unstable condition. Office Note 302, U.S. Department of Commerce, National Oceanic and Atmospheric Administration, National Weather Service, National Meteorological Center, 30 pp.

——, 1986: An economical and compatible scheme for parameterizing the stable surface layer in the medium-range forecast model. Office Note 321, U.S. Department of Commerce, National Oceanic and Atmospheric Administration, National Weather Service, National Meteorological Center, 24 pp.

Mahrt, L., 2008: Bulk formulation of the surface fluxes extended to weak-wind stable conditions. *Quart. J. Roy. Meteor. Soc.*, **134**, 1–10, doi:10.1002/qj.197.

——, 2014: Stably stratified atmospheric boundary layers. *Annu. Rev. Fluid Mech.*, **46**, 23–45, doi:10.1146/annurev-fluid-010313-141354.

——, L. Sun, W. Blumen, T. Delany, and S. Oncley, 1998: Nocturnal boundary-layer regimes. *Bound.-Layer Meteor.*, **88**, 255–278, doi:10.1023/A:1001171313493.

Medeiros, L. E., and D. R. Fitzjarrald, 2014: Stable boundary layer in complex terrain. Part I: Linking fluxes and intermittency to

an average stability index. *J. Appl. Meteor. Climatol.*, **53**, 2196–2215, doi:10.1175/JAMC-D-13-0345.1.

Miyakoda, K., and J. Sirutis, 1986: *Manual of the E-Physics*. Princeton University Press, 97 pp.

Monin, A. S., and A. M. Obukhov, 1954: Basic laws of turbulent mixing in the surface layer of the atmosphere. *Tr. Geofiz. Inst., Akad. Nauk SSSR*, **24**, 163–187.

Prigent, C., I. Tegen, F. Aires, B. Marticorena, and M. Zribi, 2005: Estimation of the aerodynamic roughness length in arid and semi-arid regions over the globe with the ERS scatterometer. *J. Geophys. Res.*, **110**, D09205, doi:10.1029/2004JD005370.

Sandu, I., A. Beljaars, P. Bechtold, T. Mauritsen, and G. Balsamo, 2013: Why is it so difficult to represent stably stratified conditions in numerical weather prediction (NWP) models? *J. Adv. Model. Earth Syst.*, **5**, 117–133, doi:10.1002/jame.20013.

Santanello, J. A., C. D. Peters-Lidard, S. V. Kumar, C. Alonge, and W.-K. Tao, 2009: A modeling and observational framework for diagnosing local land–atmosphere coupling on diurnal time scales. *J. Hydrometeor.*, **10**, 577–599, doi:10.1175/2009JHM1066.1.

Steeneveld, G.-J., 2011: Stable boundary layer issues. *Proc. ECMWF/GABLS Workshop on Diurnal Cycles and the Stable Atmospheric Boundary Layer,* Reading, United Kingdom, ECMWF, 25–36. [Available online at http://library.wur.nl/WebQuery/wurpubs/fulltext/200130.]

——, 2014: Current challenges in understanding and forecasting stable boundary layers over land and ice. *Front. Environ. Sci.*, **2**, doi:10.3389/fenvs.2014.00041.

——, M. J. J. Wokke, C. D. Groot Zwaaftink, S. Pijlman, B. G. Heusinkveld, A. F. G. Jacobs, and A. A. M. Holtslag, 2010: Observations of the radiation divergence in the surface layer and its implication for its parameterization in numerical weather prediction models. *J. Geophys. Res.*, **115**, D06107, doi:10.1029/2009JD013074.

Stoll, R., and F. Porté-Agel, 2009: Surface heterogeneity effects on regional-scale fluxes in stable boundary layers: Surface temperature transitions. *J. Atmos. Sci.*, **66**, 412–431, doi:10.1175/2008JAS2668.1.

Troen, I. B., and L. Mahrt, 1986: A simple model of the atmospheric boundary layer: Sensitivity to surface evaporation. *Bound.-Layer Meteor.*, **37**, 129–148, doi:10.1007/BF00122760.

van den Hurk, B. J. J., M. J. Best, P. A. Dirmeyer, A. J. Pitman, J. Polcher, and J. Santanello, 2011: Acceleration of land surface model development over a decade of GLASS. *Bull. Amer. Meteor. Soc.*, **92**, 1593–1600, doi:10.1175/BAMS-D-11-00007.1.

Van de Wiel, B. J. H., R. J. Ronda, A. F. Moene, H. A. R. De Bruin, and A. A. M. Holtslag, 2002a: Intermittent turbulence and oscillations in the stable boundary layer. Part I: A bulk model. *J. Atmos. Sci.*, **59**, 942–958, doi:10.1175/1520-0469(2002)059<0942:ITAOIT>2.0.CO;2.

——, A. F. Moene, R. J. Ronda, H. A. R. De Bruin, and A. A. M. Holtslag, 2002b: Intermittent turbulence and oscillations in the stable boundary layer. Part II: A system dynamics approach. *J. Atmos. Sci.*, **59**, 2567–2581, doi:10.1175/1520-0469(2002)059<2567:ITAOIT>2.0.CO;2.

——, R. J. Ronda, G. J. Steeneveld, O. K. Hartogensis, and A. A. M. Holtslag, 2007: Predicting the collapse of turbulence in stably stratified boundary layers. *Flow, Turbul. Combust.*, **79**, 251–274, doi:10.1007/s10494-007-9094-2.

——, A. F. Moene, and H. J. J. Jonker, 2012a: The cessation of continuous turbulence as precursor of the very stable nocturnal boundary layer. *J. Atmos. Sci.*, **69**, 3097–3115, doi:10.1175/JAS-D-12-064.1.

——, ——, ——, P. Baas, S. Basu, J. M. Donda, J. Sun, and A. A. Holtslag, 2012b: The minimum wind speed for sustainable turbulence in the nocturnal boundary layer. *J. Atmos. Sci.*, **69**, 3116–3127, doi:10.1175/JAS-D-12-0107.1.

Vihma, T., and Coauthors, 2014: Advances in understanding and parameterization of small-scale physical processes in the marine Arctic climate system: A review. *Atmos. Chem. Phys.*, **14**, 9403–9450, doi:10.5194/acp-14-9403-2014.

Viterbo, P., A. Beljaars, J.-F. Mahfouf, and J. Teixeira, 1999: The representation of soil moisture freezing and its impact on the stable boundary layer. *Quart. J. Roy. Meteor. Soc.*, **125**, 2401–2426, doi:10.1002/qj.49712555904.

Zheng, W., H. Wei, Z. Wang, X. Zeng, J. Meng, M. Ek, K. Mitchell, and J. Derber, 2012: Improvement of daytime land surface skin temperature over arid regions in the NCEP GFS model and its impact on satellite data assimilation. *J. Geophys. Res.*, **117**, D06117, doi:10.1029/2011JD015901.

Zilitinkevich, S., 1995: Non-local turbulent transport: Pollution dispersion aspects of coherent structure of convective flows. *Air Pollution Theory and Simulation,* H. Power, N. Moussiopoulos, and C. A. Brebbia, Eds., Vol. I, *Air Pollution III,* Computational Mechanics Publications, 53–60.

——, and P. Calanca, 2000: An extended similarity-theory for the stably stratified atmospheric surface layer. *Quart. J. Roy. Meteor. Soc.*, **126**, 1913–1923, doi:10.1256/smsqj.56617.